Solubility and vacancy-mediated interdiffusion in the Zr-Nb-Cr system

Vidur Tuli, Antoine Claisse, Luca Messina, Patrick A. Burr

Solubility and vacancy-mediated inter-diffusion in the Zr-Nb-Cr system

Vidur Tuli[a], Antoine Claisse[b], Luca Messina[c], P.A Burr[a]

[a]*School of Mechanical Engineering, University of New South Wales, Australia*
[b]*Westinghouse Electric Sweden, SE-72163 Västerås, Sweden*
[c]*Université Paris-Saclay, CEA, Service de Recherches de Métallurgie Physique, 91191, Gif-sur-Yvette, France*

Abstract

To better understand the microstructural evolution of Cr-coated Zr alloy cladding, we investigate, using density functional theory calculations, the vacancy-mediated diffusion behaviour of Zr and Nb solutes in BCC-Cr as well as Zr and Cr solutes in BCC-Nb. The calculated vacancy formation and migration energies are in good agreement with available literature, as are the self-diffusivities. We show that in BCC-Cr both Nb and Zr are faster diffusers than Cr (vacancy-mediated self-diffusion). It was also found that both Zr and Nb segregate towards vacancy sinks in BCC-Cr at normal reactor operating temperatures, but at elevated temperatures their flux is expected to be in opposite directions. In BCC-Nb, we show that Cr is a slower diffuser than Nb self-diffusion, while Zr is faster; and both Zr and Cr are expected to decorate vacancy sinks in BCC-Nb at all temperatures relevant to reactor operation. A similar behaviour is likely to occur in β-Nb phase found in Zr-Nb alloys. The implications of these findings for Cr-coated Zr alloy cladding are discussed.

1. Introduction

Following the Fukushima Daiichi accident, there has been an interest in accident tolerant fuels (ATF) in the nuclear industry [1]. The goal of developing ATFs is to develop fuel that can tolerate loss of coolant accidents for considerably longer than existing fuels while at least maintaining current fuel performance during normal operation [2–4]. Cr-coated Zr alloys are a leading candidate for ATF cladding [2, 5]. Cr is the coating of choice as it improves the cladding's oxidation and corrosion resistance for normal and accident conditions [6, 7]. Initial testing of first generation Cr-based coatings shows that it provides an exceptional balance between corrosion resistance, adhesion of the coating, neutron absorption, fretting resistance and resistance to steam oxidation [8].

The microstructural evolution at the interface between the Zr alloy substrate and the coating layer under reactor conditions is not yet fully understood. It is expected that a degree of intermixing will occur between Zr-alloy substrate and the Cr coating. This could be caused by either thermally activated equilibrium processes or by (ballistic) collision cascades. Following the collision cascades, the defects generated will also migrate, annihilate and cluster according to equilibrium thermodynamic and transport processes. In addition, the competition between dissolution and precipitation of secondary phases (e.g. $ZrCr_2$ [9]) is also dictated by thermodynamics. As inter-diffusion of these elements is a relevant part of such phenomena, we will look at the inter-diffusion of Zr and Cr. We also consider Nb as it is an important alloying addition in Zr alloy, and a potential coating material.

The solubility and diffusivity of alloying elements in α-Zr, including Cr and Nb, has been extensively studied. Previous work [9–11] showed that Cr occupies both interstitial and substitutional sites in Zr. Both interstitial and vacancy mediated diffusivities of Cr in Zr have been calculated recently [12], showing that fast interstitial diffusion dominates under equilibrium conditions, in agreement with experimental measurements by Hood *et al.* showing that Cr is an extremely fast diffuser in Zr [13, 14]. Cr in α-Zr is trapped by excess vacancies and as a result it has also been suggested that the solubility of Cr in α-Zr increases with radiation damage [10]. In addition to being trapped by vacancies, Cr is also dragged towards vacancy sinks in Zr [12]. This suggests that in a radiation damaged matrix, the flux of Cr is predicted to be substantially different than in an undefective matrix [12].

Another common alloying element used in Zr-based claddings is Nb. This includes Zirlo [15], M5 [16], Zr-1%Nb and Zr-2.5%Nb. Nb additions are known to improve the cladding's corrosion properties [17–19]. When added above its solubility limit, Nb precipitates as β-Nb particles [20, 21], and at higher concentrations still, it will form a two-phase β alloy (eg. Zr-2.5 wt% Nb alloys) [22]; but in all Zr alloys Nb retains some solubility in the α phase. Even though previously reported to be a vacancy mediated diffuser [23, 24], it has recently been suggested that it is predominantly an interstitial diffuser with the octahedral site being the most stable interstitial site [11, 25]. Interstitial diffusion mechanism of Nb in α-Zr, despite it preferentially occupying substitution sites, may be explained by the fact that the binding energy between solute and vacancy is not large enough to reduce the formation energy of the vacancy to levels competing with the low barrier for migration of interstitial Nb. Nb diffusion in Zr is reported to be 2-3 orders of magnitude faster than Zr self-diffusivity [23]. Nb has also been observed to segregate heavily towards grain boundaries in Zirlo [26], suggesting diffusion towards vacancy sinks.

On the other hand, diffusion behaviour of Zr and Nb solutes

in body-centered-cubic (BCC) Cr, and that of Zr and Cr solutes in BCC-Nb has hardly been studied. Here we use ab-initio atomic-scale simulations to shed light on the role of vacancies on the solubility, mobility and segregation of Zr and Nb solutes in BCC-Cr, and Cr and Zr solutes in BCC-Nb. We combine this information with existing knowledge of Cr and Nb solutes in hexagonal-close-packed (HCP) Zr, to paint a comprehensive picture of the equilibrium thermodynamic and kinetic processes that govern the inter-diffusion at the Zr-alloy/Cr-coating interface, thus shedding light on the microstructural evolution of this system.

2. Methodology

In the framework of thermodynamics of irreversible processes, the diffusion coefficients of each species in the system can be derived from the Onsager coefficients (L^{ss}, L^{sv}, L^{vv}). These coefficients are tensorial transport coefficients that relate solute and vacancy chemical potential gradients, μ^s and μ^v, to solute and vacancy fluxes, j^s and j^v [27].

$$j^s = -L^{ss}\nabla\mu^s - L^{sv}\nabla\mu^v \tag{1}$$

$$j^v = -L^{vv}\nabla\mu^v - L^{sv}\nabla\mu^s \tag{2}$$

In the dilute limit, the solute diffusivity D_s is directly proportional to L^{ss} [28, 29] .

$$D_s = \frac{k_B T \Omega L^{ss}}{c^s} \tag{3}$$

where k_B is the Boltzmann constant, T is the temperature, Ω is the volume per atom and c_s is the solute concentration. When only one diffusion mechanism is at play (or dominates), the solute diffusivity can also be expressed in Arrhenius form

$$D_s = D_0^s e^{\frac{-Q}{k_B T}} \tag{4}$$

where D_0^s is the pre-exponential factor, containing all entropy terms, and Q is the activation energy required for diffusion.

We quantify the vacancy drag of solutes by calculating the drag ratio (DR)

$$DR = L^{sv}/L^{ss} \tag{5}$$

A positive drag ratio means that the vacancy drags the solute along with it, on the other hand a negative ratio does not imply that the solute will segregate away from vacancy sinks. To ascertain this, one must consider the partial diffusion coefficient ratio (PDR), which compares solute to solvent diffusivity. In the dilute limit, the PDR is related to transport coefficients by the following expression [30]:

$$d_{sv}/d_{av} = \frac{l_{as} + l_{ss}}{L^0_{vv}} \tag{6}$$

where, a refers to the solvent, s refers to the solute, v refers to the vacancy, d refers to the partial diffusion coefficient, and

$$l_{as} = -l_{ss}(1 + DR) \tag{7}$$

$$l_{ss} = L_{ss}/c_s \tag{8}$$

Solute drag by vacancies, thus solute enrichment at vacancy sinks, happens when d_{sv} is negative (d_{av} is always positive), which in turn means the PDR is negative. In case of solute and vacancy diffusing in opposite directions (inverse Kirkendall effect), the PDR is always positive. However, solute enrichment at sinks may still occur when the solute and solvent diffuse in the same direction but the solute diffuses slower than the host matrix atoms or $0 < \text{PDR} < 1$. Solute depletion at sinks happens when the PDR is positive and solute atoms diffuses faster than the matrix atoms, which means $d_{sv} > d_{av}$ or PDR>1

The Onsager coefficients were calculated using both the Onsager code by Dallas Trinkle [31, 32] and the KineClue code by Schuler *et al.* [33]. Within numerical error, the two codes yielded consistent results despite differences in the way the cut-off for solute-vacancy correlations is calculated. The solute-vacancy binding energies, the migration energy (E^m) for each jump, and the associated attempt frequencies were calculated using DFT simulations. We calculated the solute binding energies to vacancies up to the 10th nearest neighbour position, and considered all interactions up to the 5th nearest neighbour to build the network of transition rates. Fig 1 shows the vacancy mediated jump network for a solute in a BCC structure with interactions extending up to the 5th nearest neighbour. In a dilute binary alloy, the vacancy jump in the dilute limit is denoted as ω_0 (not shown in the figure) and the solute-vacancy exchange jump is denoted as ω_2.

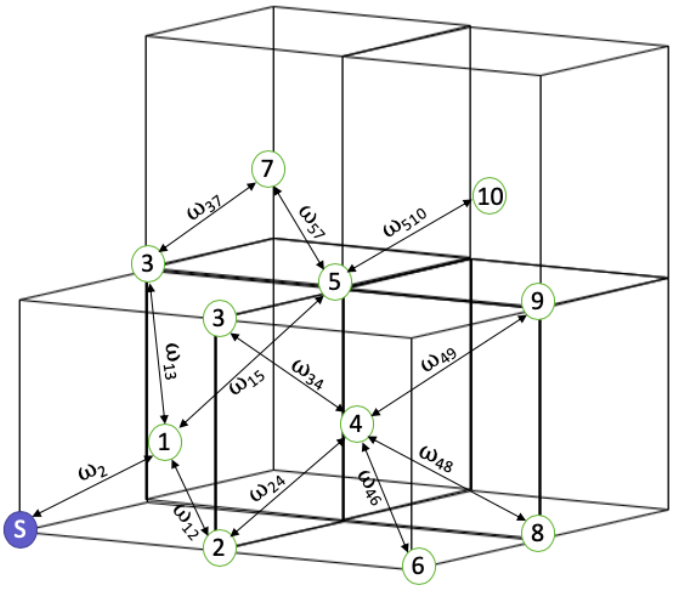

Figure 1: Compendium of vacancy jumps in the vicinity of the solute atom in a BCC lattice. The numbers in the circles refer to the nearest neighbour position with respect to the solute s. Each ω represents a symmetrically unique jump, following the nomenclature from [30]

Cr at room temperatures and above is paramagnetic [34]. This disordered magnetic structure is computationally difficult to model [35, 36], thus we considered two bounding magnetic ordering of BCC-Cr: anti-ferromagnetic (AFM) and non-magnetic

(no spin polarisation, NM). We neglected possible difference in binding and migration energy due to different spins. Considering that the binding energy and diffusivity results of the two bounding cases were not too different, we expect paramagnetic structure to exhibit similar results.

DFT simulations were carried out using the VASP code [37, 38] with the PBE exchange correlation functional [39] and a consistent plane wave cut off energy of 350 eV. BCC-Cr and BCC-Nb were modelled using 128 atom supercells with $4 \times 4 \times 4$ k-point grid. Atoms were described with PAW pseudopotentials from the VASP 5.4 repository. Partial occupancy were treated with a first-order Methfessel-Paxton smearing function of width 0.1 eV. The equilibrium lattice parameters for BCC-Cr were found to be 2.84 Å(NM) and 2.86 Å(AFM). These are in agreement with values reported in literature — 2.85 Å(NM) and 2.87 Å(AFM) [40]. The equilibrium lattice parameter for BCC-Nb was found to be 3.32 Å, which is in agreement with the value of 3.29 Å reported by Jiang *et al.* [41]. All point defects were then modelled using the equilibrium lattice parameters.

Defect formation energies (E^f) were calculated using:

$$E^f = E_{\mathrm{d}}^{\mathrm{DFT}} - E_{\mathrm{p}}^{\mathrm{DFT}} \pm \sum_i \mu(i) \tag{9}$$

where $E_{\mathrm{d}}^{\mathrm{DFT}}$ and $E_{\mathrm{p}}^{\mathrm{DFT}}$ are the total energies from the defective and perfect DFT simulations and μ_i is the chemical potential of all species i that are added or removed from the perfect crystal to form the defect. The chemical potential μ is calculated as the DFT energy per atom of the metallic elements in their ground state.

The solute-vacancy binding energy was calculated using the following equation

$$E^b = E_{\mathrm{sv}}^f - (E_{\mathrm{s}}^f + E_{\mathrm{v}}^f) \tag{10}$$

where E^b is the binding energy, E_{sv}^f is the formation energy of the defect cluster containing a solute atom and a vacancy, E_{s}^f is the formation energy of the isolated solute defect and E_{v}^f is the formation energy of a vacancy.

The E^m of each jump was calculated as the saddle point in the minimum energy paths between two stable defect sites. This was calculated using the climbing nudged elastic band method (cNEB) as implemented in the VTST-modified version of VASP [42, 43]. The cNEBs were simulated with a minimum of 5 images, and up to 9 images. For E^m of jumps that do not involve the 1st, 2nd or 3rd nearest neighbour we use the Final Initial State Energy (FISE) approximation [30] as it yields sufficiently accurate results, see appendix for details.

The jump's attempt frequencies were calculated by dividing hopping atom's vibrational eigenfrequencies in the ground state configuration by the vibrational frequencies in the transition state, following Vineyard's expression [44]

$$\nu = \frac{\prod_{n=1}^{3} \nu^{GS}}{\prod_{n=1}^{2} \nu^{TS}} \tag{11}$$

The vibrational frequencies were computed with pertubation theory (phonon calculations) where only the hopping atom's degrees of freedom were considered. Vibrational frequencies of the entire supercell for each state are computationally demanding and result in high uncertainty due to the large number of frequencies in both the numerator and denominator [30]. Therefore, we considered the vibrational frequencies of the hopping atom only, which has shown to yield accurate and reliable results in a range of systems [11, 12, 30, 45].

3. Results and Discussion

The E^f and E^m in BCC-Cr and BCC-Nb are presented in Table 1, and are in excellent agreement with available literature. There is a significant discrepency between the vacancy migration energy we obtain in BCC-Nb and the results published by Nguyen-Manh [46]. However, our results are in better agreement with more recent modelling results published by Ma et al. who reported a value of 0.64 eV [47] and experimental results published by Schultz who reported a value of 0.55 eV [48].

Table 1: Vacancy formation and migration energy in BCC-Cr and BCC-Nb

		BCC-Cr		BCC-Nb
		NM	AFM	
E^{f}	Current Work	2.73 eV	2.96 eV	2.68 eV
	Literature (modelling)	2.64 eV [46]	3.02 eV [47]	2.6-3.0 eV [46, 47, 49, 50]
	Literature (experiment)	-	-	2.70 eV [48]
E^{m}	Current Work	0.90 eV	1.10 eV	0.44 eV
	Literature (modelling)	0.91 eV [46]	1.11 eV [47]	0.90 eV [46], 0.64 eV [47]
	Literature (experiment)	-	-	0.55 eV [48]

The self-diffusivity of Cr and Nb, calculated considering just the vacancy exchange mechanism, and using vacancy formation entropy values of 2.25 k_B and 2.2 k_B [51] respectively, are shown in Fig 2. The self-diffusivity results are in excellent agreement with experimental bulk-diffusivity results [52, 53]. Literature available suggested that the self diffusion of Cr can be represented by mono-vacancy diffusion up to 1700-2000 K [54–57]. The experimental results reported for Nb self diffusion account for both monovacancy and divacancy diffusion. For monovacancy diffusion, Einzinger *et al.* [53] report the pre-exponential factor as $8 \pm 3 \times 10^{-3}$ cm^2/s and the activation energy required for diffusion as 3.64 eV. These are in reasonable agreement with the values of 0.3×10^{-3} cm^2/s and 3.14 eV respectively, obtained from our modelling work. The reported activation energy for divacancy diffusion is 4.54 eV,

leading to different slope of the diffusivity results in Fig 2b. Moreover, it is worth noting that our calculations are performed in the ground state (0K) and are extrapolated to the temperature range in question through harmonic approximation. The further we extrapolate the ground state results, the weaker the assumption of harmonic behaviour become. At high temperature the effect of thermal expansion, not accounted for here, becomes more important. Similarly anharmonic effects become more pronounced [58, 59]. Furthermore, the existence of impurities in the samples could account for the remaining discrepancy [60].

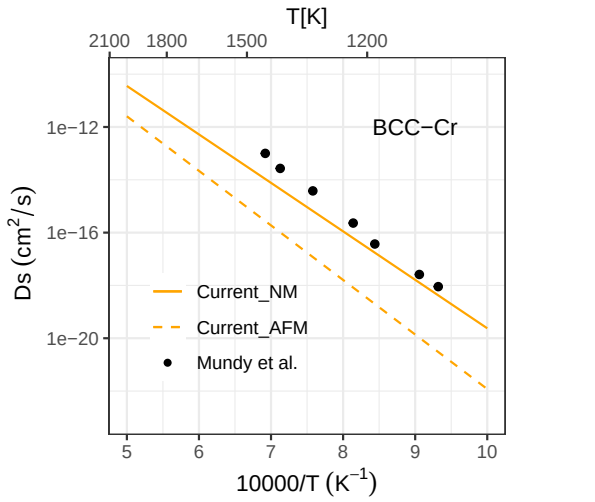

(a) Cr self diffusion

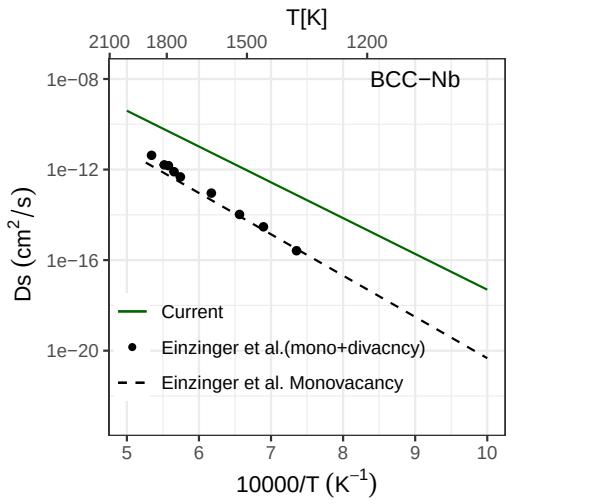

(b) Nb self diffusion

Figure 2: Comparison between calculated and experimental self-diffusivity in BCC-Cr and BCC-Nb [52, 53]

The formation energies of substitution and interstitial defects in BCC-Cr and BCC-Nb are summarised in Table 2. The table also contains defect formation energies in HCP-Zr to provide a wholistic picture of the Zr-Nb-Cr system. The Cr defect formation energies in HCP-Zr are from Burr *et al.* [10], whereas the Nb defect formation energies in HCP-Zr are from Xin *et al.* [61]. It is evident that all solutes are preferentially accommodated as substitutional species in BCC-Cr and BCC-Nb. This accommodation as substitutional species is expected in BCC-Cr, given that the metallic radii of Zr (161 pm) and Nb (147 pm) are significantly larger than that of Cr (128 pm) [62].

Considering the high formation energy for interstitial defects, modelling was not carried out for interstitial diffusion as it is not expected to contribute meaningfully to equilibrium diffusion (i.e. not driven by ballistic collisions). It was observed that dumbbells only form in the <110> configuration. This is also expected considering that the <110> direction is the most common dumbbell orientation in BCC metals [63, 64]. Conversely, crowdion defects with a longer range one-dimensional structure form along the <111> directions in BCC-Cr, while in BCC-Nb they form in the <100> and <111> direction. We expect the energy of these defects to be more sensitive to the choice of supercell size than other point defects [45, 65].

Even though this study focuses on vacancy mediated diffusion, under irradiation damage interstitial diffusion becomes as important as vacancy-mediated diffusion. Thus, based on the interstitial sites observed, we can infer the possible diffusion pathways for interstitial diffusion of solutes in BCC-Cr and BCC-Nb, once the defects are formed as a consequence of collision cascades. Since the <111> crowdion site is the lowest energy interstitial site in both BCC-Cr and BCC-Nb, diffusion along the crowdion direction is likely to be fast. However, it is noted that as the crowdion moves forwards it effectively becomes a self-interstitial atom, with the solute atom moving only one site, until a further crowdion defect crosses the path of the solute. In BCC-Nb crowdion may form also along the <100> direction, but at considerably higher energy. Considering that the dumbbell configuration has only slightly higher energy compared to the <111> crowdion site in BCC-Cr (0.4-0.7 eV), we can expect this configuration to contribute significantly to the overall solute diffusion, possibly as an intermediate jump between two different <111> crowdions. Similar behaviour is expected for Zr in BCC-Nb. Cr in BCC-Nb, which is only stable on the octahedral site, is expected to have a simple (and isotropic) interstitial diffusion pathway from octahedral to octahedral site, until it is trapped by a vacancy or other defect. Conversely, in BCC-Cr, the octahedral site is not likely to contribute significantly to diffusion of Zr and Nb owing to its high formation energy. It is worth noting that the interstitial diffusion pathways discussed here are based on just the formation energies of the interstitial sites. However, the actual contribution of each site will depend on the migration barrier of interstitial defects as well (which we do not look at in this work).

Modelling was carried out for vacancy mediated diffusion of Zr and Nb in BCC-Cr and Zr and Cr in BCC-Nb. Fig 3 shows the binding energies of solutes to vacancies as a function of neighbour positions. Both Zr and Nb are found to be strongly bound to Cr vacancies in the 1st nearest neighbour position, but exhibit near-zero binding at all other distances from the solute (Fig 3a). This distinct lack of attraction between vacancies and solutes past the first nearest neighbour suggests that the diffusion of Cr vacancies is not affected by the presence of Zr or Nb atoms as long as they stay further away than the 1st nearest

Table 2: Formation energies of extrinsic defects in BCC-Cr, BCC-Nb and HCP-Zr. Self-interstitial defects are not included as they are not relevant to the current study.

Solute	Site	BCC-Cr		BCC-Nb	HCP-Zr
		NM	AFM		
Nb	Octahedral	10.13 eV	14.94 eV	N/A	2.56 eV [61]
	Dumbbell <110>	9.18 eV	9.34 eV		-
	Crowdion <111>	8.47 eV	8.86 eV		-
	Substitution	0.82 eV	0.88 eV		0.67 eV [61]
Cr	Octahedral	N/A	N/A	3.57 eV	1.88 eV [10]
	Dumbbell <110>			not stable	-
	Crowdion			not stable	2.06 eV [10]
	Substitution			0.29 eV	1.89 eV [10]
Zr	Octahedral	10.80 eV	10.84 eV	5.74 eV	N/A
	Dumbbell <110>	9.89 eV	10.03 eV	4.89 eV	
	Crowdion <111>	9.31 eV	9.68 eV	4.61 eV	
	Crowdion <100>	not stable	not stable	5.28 eV	
	Substitution	1.634 eV	1.77 eV	0.29 eV	

neighbour configuration.

In BCC-Nb, Zr and Cr solutes exhibit markedly different interaction with Nb vacancies (Fig 3b). Zr exhibits the strongest binding to vacancies in the 1st nearest neighbour position while Cr is most strongly bound to vacancies only in the 2nd nearest neighbour position. Cr also exhibits repulsion to vacancies at most other distances. The binding energies of both the solutes exhibits stark symmetry and this may be due to the opposite difference in radii between the solutes and Nb (+14 pm for Zr and −19 pm for Cr [62]).

Fig 4 and 5 show the E^m obtained using the cNEB method for diffusion in BCC-Cr and BCC-Nb respectively. The difference in E^m along the migration pathways between different solutes decreases as the solute moves further away than the vacancy. This is expected as we get progressively further away from the solute, the vacancy jumps profiles approach those of the pure BCC metals.

The distance between the Zr solute initial and final position in the solute-vacancy jump (ω_2) is small in both BCC-Cr and BCC-Nb. This is expected as it is an oversized solute and as a result it is placed closer to the vacancy at the start of the jump. The barrier for the (ω_2) jump is very low, which causes on the one-hand easier solute-vacancy exchange, but on the other hand a strong correlation effect that compensates for the low barrier. It is also worth noting that we do not observe any *oversized solute atom mechanism* as reported in [66, 67]. That is, in the present study, the solute-vacancy complex does not relax to a configuration where the solute sits in the middle of two half-vacancies.

Fig 6 shows the diffusivity of solutes in both BCC-Cr and BCC-Nb at equilibrium vacancy concentrations, and the D_0 and Q values for all solutes are provided in Table 3. Both Zr and Nb exhibit faster diffusion that Cr self-diffusion in BCC-Cr (Fig 6a). The effect of magnetic ordering of BCC-Cr on diffusivity is found to be small ($\sim$ 10 cm^2/s at high temperature $\sim$ 100 cm^2/s at lower temperatures) with the NM structure providing the upper bound and AFM structure providing the lower bound.

It is also observed that Cr exhibits slower diffusion than Zr and Nb self-diffusion in BCC-Nb (Fig 6b). This can be explained by the repulsion of Cr with vacancies at the 1st NN position and the high barrier for the solute-vacancy exchange jump.

Fig 6b also shows that the experimental diffusivity for Cr in BCC-Nb [68] is in excellent agreement with the current predictions (activation energies of 3.67 eV and 3.62 eV, respectively), while for Zr in BCC-Nb [60] there is some discrepancy. The higher experimentally measured activation energy (3.93 eV, compared to 2.92 eV for the current study) could be due to a number of reasons. The first being, as the authors have acknowledged themselves, errors could have been introduced due to the challenge of observing radioactive impurity levels with the experimental techniques used. Another reason could be the possibility of divacancy mechanism playing a role in the diffusion like it did in Nb self-diffusion. Divacancy mechanism would have a higher activation energy as reported for Nb self-diffusion. Finally, high temperature effects being ignored in modelling work presented here could lead to further discrepancy between the two set of results. However, experimentally Zr diffusivity is shown to be $\sim$ 1 order of magnitude higher than Nb self-diffusivity at high temperatures [60, 69], which is consistent with modelling results.

Table 4 shows a direct comparison between the Q values obtained from our work against the activation energy values obtained by the classical approach (Q_{classic}). In the classical approach:

$$Q_{\text{classic}} = E_f + E_m^* + E_b^* \tag{12}$$

where E_f is the vacancy formation energy, E_m^* is the migration energy for the ω_2 jump and E_b^* is the solute binding energy to the vacancy in the 1st NN position. It is clear that where ω_2 is the rate limiting step (for Cr in BCC-Nb), the agreement is excellent. However, when ω_2 is significantly faster than other

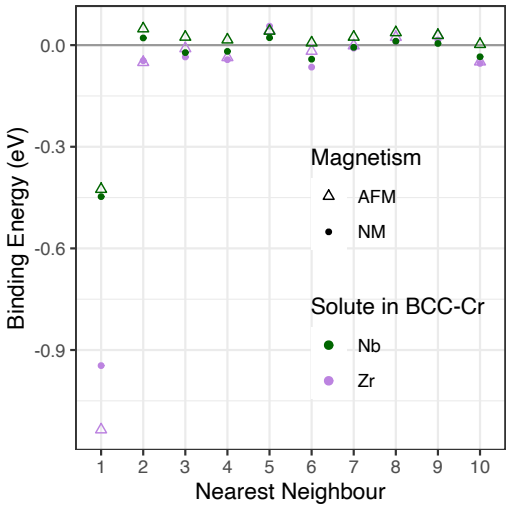

(a) BCC-Cr

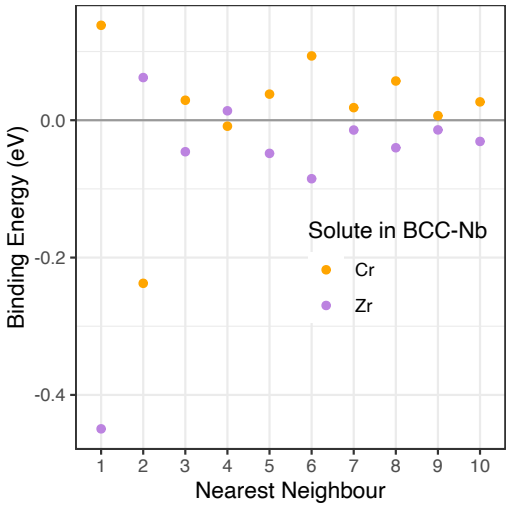

(b) BCC-Nb

Figure 3: Binding energies of solutes to vacancies in BCC-Cr and BCC-Nb. Positive binding energy denotes repulsive interactions while negative binding energy denotes attractive interactions.

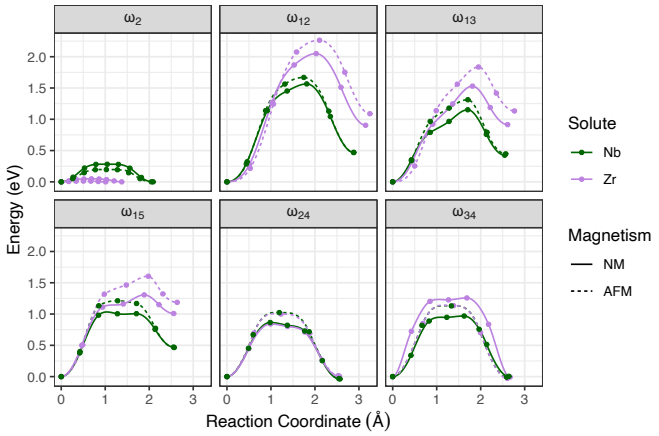

Figure 4: Vacancy migration energy with Nb and Zr solutes in BCC-Cr

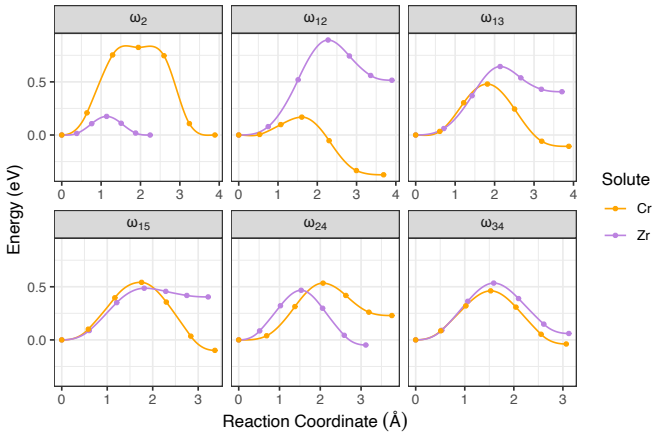

Figure 5: Vacancy migration energy with Cr and Zr solutes in BCC-Nb

jumps, correlation between reconfiguration, exchange and escape jumps becomes important. This highlights the importance of performing a thorough analysis of vacancy-solute interactions in cases where the classical approach would fail.

Fig 7 shows the drag ratios and PDR of the solutes in BCC-Cr and BCC-Nb. The drag ratios of solutes in both BCC-Cr and BCC-Nb start off positive and large and reduce with increasing temperature. The decline in drag ratios is more dramatic in BCC-Nb at T > 800 K. In BCC-Cr the behaviour of Nb and that of Zr solutes are different and we observe a more rapid decline in the Nb drag ratio in the 600–1000 K temperature range. Since the Nb drag ratio becomes negative, it suggests that under elevated temperatures of 700–900 K (e.g. dry storage) Nb would diffuse away from vacancy sinks. The PDR of Nb in BCC-Cr, shown in Fig 7c, confirms that there would be depletion of Nb solute at vacancy sinks at these elevated temperatures [30], as PDR>1. This means that the flux of Nb will be in opposite direction to that of Zr in BCC-Cr in the temperature range 700 K < T < 1200 K as far as the vacancy mechanism is concerned. The rate of change of the drag ratio of Nb as a function of temperature is also greater than that of Zr, suggesting that Nb redistribution is more sensitive to relatively small variations in temperature, which may then affect the performance of the coating after prolonged period of radiation damage and thermal cycling.

Both solutes (Zr and Cr) also exhibit a positive drag ratio in BCC-Nb at all temperatures of concern. This suggests that, like Zr in BCC-Cr, both solutes are expected to decorate vacancy sinks in BCC-Nb (Fig 7b). The PDR, shown in Fig 7d, further confirms this finding as both Zr and Cr have a PDR < 1 in BCC-Nb. Since the PDR for Cr is really small at all temperatures shown ($\sim -10^{-07}$ to -10^{-02}), Cr drag by vacancies and enrichment at sinks, although active, will be negligible compared to Zr.

The behaviour of these solutes in BCC-Nb and BCC-Cr is in stark contrast to that of Cr and Nb in HCP-Zr. Both solutes are predominantly interstitial diffusers in HCP-Zr, and both are significantly faster than Zr self-diffusion. However, the diffusion behaviour of Cr in the HCP-Zr matrix is expected to change with increase in irradiation induced damage, leading to a con-

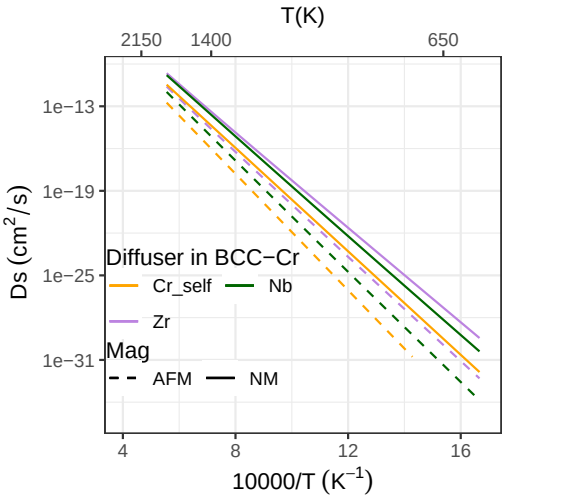

(a) BCC-Cr

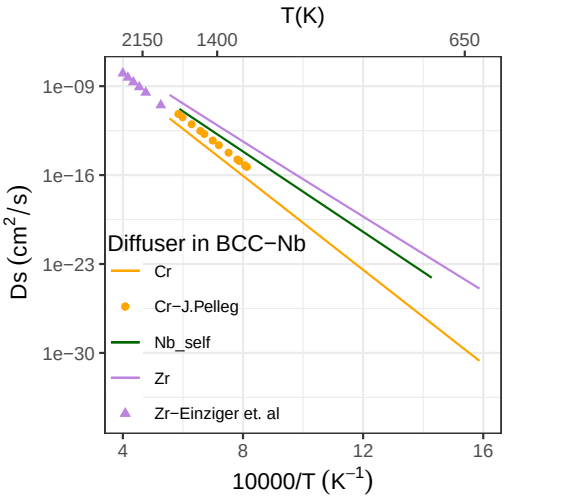

(b) BCC-Nb

Figure 6: Diffusivity of Nb, Cr and Zr solutes in BCC-Cr and BCC-Nb

siderably slower diffusion, and significant vacancy drag [12].

Considering the β-Nb phase in Zr-Nb alloys, or a potential Nb coating, we can infer the following behaviour from the current results. Firstly, Cr has a much lower solution energy in BCC-Nb (0.29 eV) compared to HCP-Zr (1.89 eV), see Table 1. This suggests that, in Zr-Nb alloys, Cr solutes would have a preference to dissolve in the β-Nb phase compared to the bulk of the alloy. However, we know that the $ZrCr_2$ is stable in both the C14 and C15 structures [9, 70] with a much lower formation enthalpy of -0.3 eV/formula unit [9, 71]. This means that the precipitation of $ZrCr_2$ phase, typically with significant Fe content in the form of $Zr(Fe,Cr)_2$, will compete with the Cr dissolution in the β-Nb phase. We also expect both Zr and Cr solutes in the β-Nb phase to segregate towards vacancy sinks. However, looking at the Cr-vacancy repulsion at the 1^{st} nearest neighbour position, the higher ω_2 barrier, and the small PDR value, the transport of Cr in Nb will be limited. Radiation damage induced dissolution of β-Nb phase may lead to increased

Table 3: Diffusivity equation coefficients obtained by performing an Arrhenius fit to the diffusion coefficients shown in Fig 6

Solute	Solvent	D_0 (cm^2/s)	Q (eV)
Zr	Cr(AFM)	0.05	3.69
Zr	Cr(NM)	0.04	3.34
Nb	Cr(AFM)	0.07	3.89
Nb	Cr(NM)	0.08	3.49
Cr	Nb	0.06	3.67
Zr	Nb	0.04	2.92

Table 4: Comparison between reported Q and $Q_{classic}$. Excellent agreement observed for Cr in BCC-Nb, where ω_2 is the rate limiting step.

Solute	Solvent	Q (eV)	E_f (eV)	E_m (eV)	E_b (eV)	$Q_{classic}$ (eV)
Zr	Cr(AFM)	3.69	2.96	0.05	-1.13	1.88
Zr	Cr(NM)	3.34	2.73	0.05	-0.95	1.83
Nb	Cr(AFM)	3.89	2.96	0.19	-0.43	2.72
Nb	Cr(NM)	3.49	2.73	0.28	-0.45	2.56
Cr	Nb	3.67	2.69	0.84	0.14	3.67
Zr	Nb	2.92	2.69	0.18	-0.45	2.42

concentration of Nb in the bulk of the alloy and consequently increased decoration of vacancy sinks in the α-Zr matrix.

Considering the interface between Cr coating and the Zr based alloy, it is reasonable to assume that Zr or Nb atoms will be displaced in to the coating layer by a few Å due to inter-diffusion or ballistic intermixing. However, the formation of $ZrCr_2$ phase, typically with Fe in the form of $Zr(Fe,Cr)_2$ has been extensively reported at the interface between Cr coating and Zr substrate, making it a more likely outcome of the inter-diffusion and making it less likely for Zr and Nb solutes to displaced through the intermetallic layer of thickness ranging from 1-2 μm [8, 72, 73]. We can still expect ballistic damage to cause redistribution of Zr and Nb solutes in to the Cr coating, either from the host cladding or the intermetallics formed at the interface between the Zr substrate and the Cr coating. At normal reactor operating temperatures (573-673 K), we expect both Nb and Zr solutes to segregate towards vacancy sinks in the Cr coating (e.g. grain boundaries and dislocation loops). However, under elevated temperatures (700 K < T < 1200 K) we expect the flux of Nb to be in the opposite direction to that of Zr, with Zr decorating vacancy sinks and Nb moving away from vacancy sinks. We suggest that under normal reactor operating temperature, vacancy sinks in the coating material will have an increased likelihood of intermetallic formation due to increased concentration of solute.

4. Conclusion

We use DFT calculations to better understand the solubility and inter-diffusion behaviour in the Zr-Nb-Cr system. The DFT calculation supports the following conclusions:

- In BCC-Cr, Zr and Nb solutes are preferentially accommodated as substitutional species. Same can be said for Zr and Cr solutes in BCC-Nb.
- Zr is strongly bound to vacancies in the 1st nearest neighbour position in both BCC-Cr and BCC-Nb followed by much weaker binding at all other positions. Nb in BCC-Cr exhibits a similar behaviour. However, Cr in BCC-Nb exhibits strong binding to vacancies in the 2nd nearest neighbour position and repulsion in most other positions.
- In BCC-Cr, both Zr and Nb are faster diffusers than Cr, with both solutes likely to decorate vacancy sinks up to temperatures of 700 K. Above 700 K, Zr and Nb solutes exhibit flux in opposite directions with Zr following vacancy flux, while Nb displays inverse Kirkendall effect.
- Cr is a slower diffuser than Zr and Nb self-diffusion in β-Nb. Both solutes are dragged by vacancies even at high temperature.

The current work lays the foundation of understanding the intermixing in Cr coated Zr alloys. The findings clarify the atomic scale transport behaviour of alloying elements in the alloy. Further work is required to look at the diffusivity of solutes in solid solutions found in these alloys. This is important as solid solutions, such as β-Zr and β-Nb phases, are quite commonly observed in Zr alloys.

5. Acknowledgements

We would like to thank Westinghouse Electric (Sweden) for providing financial support to enable work on this project. This research was supported by an Australian Government Research Training Program (RTP) Scholarship. This work was undertaken with the assistance of resources and services from the National Computational Infrastructure (NCI), which is supported by the Australian Government; the Multi-modal Australian ScienceS Imaging and Visualisation Environment (MASSIVE); the Pawsey Supercomputing Centre, which is supported by the Australian Government and the Government of Western Australia; and was enabled by Intersect Australia Limited. Learn more at www.intersect.org.au.

A. Appendix

Fig A.1 compares the energies obtained using the FISE-estimated transition state and the NEB-simulated transition state in BCC-Cr with Zr as solute. It is evident that the difference becomes negligibly small for jumps further away than the third nearest neighbour from the solute. We expect other clusters to converge to dilute behaviour faster than $[Zr_{Cr}{:}V_{Cr}]^{BCC\text{-}Cr}$. This is due to the fact that Zr in Cr causes the largest compressive stress. This means that at long distances FISE for other clusters should be as good as, or better than, FISE for $[Zr_{Cr}{:}V_{Cr}]^{BCC\text{-}Cr}$

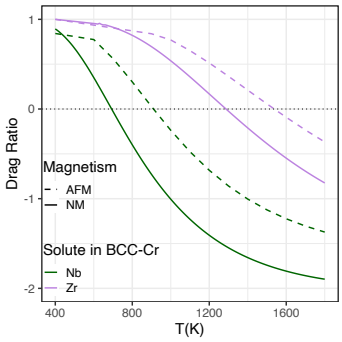

(a) Drag ratio of Zr and Nb in BCC-Cr

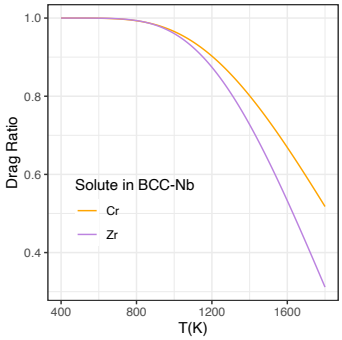

(b) Drag ratio if Zr and Cr in BCC-Nb

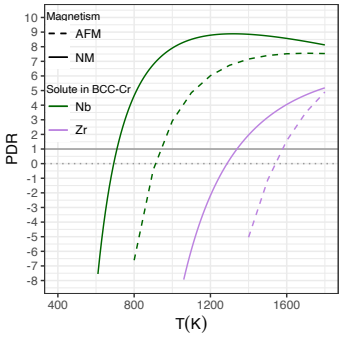

(c) PDR of Zr and Nb in BCC-Cr

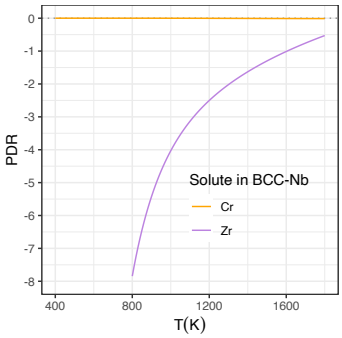

(d) PDR of Zr and Cr in BCC-Nb

Figure 7: Drag ratios and partial diffusion coefficient ratio of solutes in BCC-Cr and BCC-Nb as a function of T

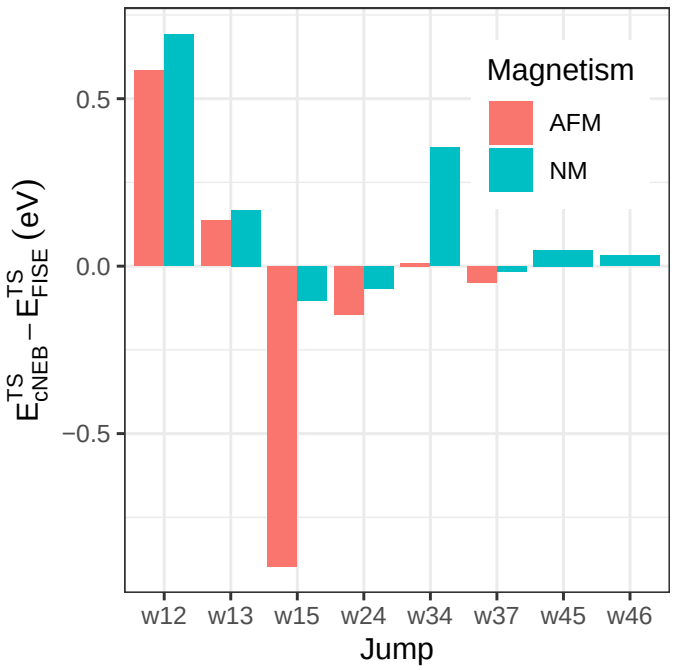

Figure A.1: Difference between migration energies from cNEB and FISE for Zr in BCC-Cr

References

1. IAEA. *Accident Tolerant Fuel Concepts for Light Water Reactors* tech. rep. October (IAEA, Vienna, 2016), 13–16.
2. Terrani, K. A. Accident tolerant fuel cladding development: Promise, status, and challenges. *Journal of Nuclear Materials* **501,** 13–30 (2018).
3. Goldner, F. *Overview of the accident-tolerant fuel development* tech. rep. March 2011 (Department of Energy (DOE), US, 2013), 14.
4. Zinkle, S. J., Terrani, K. A., Gehin, J. C., Ott, L. J. & Snead, L. L. Accident tolerant fuels for LWRs: A perspective. *Journal of Nuclear Materials* **448,** 374–379 (2014).
5. Tang, C., Stueber, M., Seifert, H. J. & Steinbrueck, M. Protective coatings on zirconium-based alloys as accident-Tolerant fuel (ATF) claddings. *Corrosion Reviews* **35,** 141–165 (2017).
6. Bischoff, J., Delafoy, C., Vauglin, C., Barberis, P., Roubeyrie, C., Perche, D., Duthoo, D., Schuster, F., Brachet, J. C., Schweitzer, E. W. & Nimishakavi, K. AREVA NP's enhanced accident-tolerant fuel developments: Focus on Cr-coated M5 cladding. *Nuclear Engineering and Technology* **50,** 223–228 (2018).
7. Park, J. H., Kim, H. G., Park, J. y., Jung, Y. I., Park, D. J. & Koo, Y. H. High temperature steam-oxidation behavior of arc ion plated Cr coatings for accident tolerant fuel claddings. *Surface and Coatings Technology* **280,** 256–259 (2015).
8. Brachet, J. C., Idarraga-Trujillo, I., Flem, M. L., Saux, M. L., Vandenberghe, V., Urvoy, S., Rouesne, E., Guilbert, T., Toffolon-Masclet, C., Tupin, M., Phalippou, C., Lomello, F., Schuster, F., Billard, A., Velisa, G., Ducros, C. & Sanchette, F. Early studies on Cr-Coated Zircaloy-4 as enhanced accident tolerant nuclear fuel claddings for light water reactors. *Journal of Nuclear Materials* **517,** 268–285 (2019).
9. Lumley, S. C., Murphy, S. T., Burr, P. A., Grimes, R. W., Chard-Tuckey, P. R. & Wenman, M. R. The stability of alloying additions in Zirconium. *Journal of Nuclear Materials* **437,** 122–129 (2013).
10. Burr, P. A., Wenman, M. R., Gault, B., Moody, M. P., Ivermark, M., Rushton, M. J., Preuss, M., Edwards, L. & Grimes, R. W. From solid solution to cluster formation of Fe and Cr in α-Zr. *Journal of Nuclear Materials* **467,** 320–331 (2015).
11. Lu, H. J., Wu, H., Zou, N., Lu, X. G., He, Y. L. & Morgan, D. First-principles investigation on diffusion mechanism of alloying elements in dilute Zr alloys. *Acta Materialia* **154,** 161–171 (2018).
12. Jain, A. C., Burr, P. A. & Trinkle, D. R. First-principles calculations of solute transport in zirconium: Vacancy-mediated diffusion with metastable states and interstitial diffusion. *Physical Review Materials* **3,** 33402 (2019).
13. Hood, G. M. & Schultz, R. J. Chromium diffusion in α-zirconium, Zircaloy-2 and Zr-2.5Nb. *Journal of Nuclear Materials* **200,** 141–143 (1993).
14. Balart, S. N., Varela, N. & de Tendler, R. H. 51Cr diffusion in α-Zr single crystals. *Journal of Nuclear Materials* **119,** 59–66 (1983).
15. Sabol, G., Kilp, G., Balfour, M. & Roberts, E. Development of a Cladding Alloy for High Burnup. *Zirconium in the Nuclear Industry: Eighth International Symposium,* 227–227 (2008).
16. Garner, G., Hilton, B. & Mader, E. *2007 LWR Fuel Performance/Top Fuel : September 30th - October 3, 2007, San Francisco, California.* in *2007 LWR Fuel Performance Meeting / TopFuel 2007 'Zero by 2010'* (American Nuclear Society, 2007).
17. Jeong, Y. H., Kim, H. G., Kim, D. J., Choi, B. K. & Kim, J. H. Influence of Nb concentration in the α-matrix on the corrosion behavior of Zr-xNb binary alloys. *Journal of Nuclear Materials* **323,** 72–80 (2003).
18. Jeong, Y. H., Lee, K. O. & Kim, H. G. Correlation between microstructure and corrosion behavior of Zr-Nb binary alloy. *Journal of Nuclear Materials* **302,** 9–19 (2002).
19. Kim, H. G., Park, S. Y., Lee, M. H., Jeong, Y. H. & Kim, S. D. Corrosion and microstructural characteristics of Zr-Nb alloys with different Nb contents. *Journal of Nuclear Materials* **373,** 429–432 (2008).
20. Park, J. Y., Choi, B. K., Jeong, Y. H. & Jung, Y. H. Corrosion behavior of Zr alloys with a high Nb content. *Journal of Nuclear Materials* **340,** 237–246 (2005).
21. Banerjee, S., Vijayakar, S. J. & Krishnan, R. Precipitation in zirconium-niobium martensites. *Journal of Nuclear Materials* **62,** 229–239 (1976).
22. Perovic, A., Perovic, V., Weatherly, G. G., Purdy, G. R. & Fleck, R. G. A study of the distribution of Nb and Fe in two-phase Zr-2.5 wt% Nb alloys. *Journal of Nuclear Materials* **199,** 102–111 (1993).
23. Hood, G. M., Zou, H., Schultz, R. J. & Matsuura, N. Nb diffusion in single-crystal α-Zr. *Defect and Diffusion Forum* **143-147,** 55–60 (1997).
24. Tendler, R. & Abriata, J. P. Atomic size and fast diffusion of metallic impurities in zirconium. *Journal of Nuclear Materials* **150,** 251–258 (1987).
25. Zou, H., Hood, G. M., Roy, J. A., Schultz, R. J. & Jackman, J. A. Hf diffusion in dilute Fe-free Zr(Nb) alloys. *Philosophical Magazine A: Physics of Condensed Matter, Structure, Defects and Mechanical Properties* **71,** 901–906 (1995).
26. Hudson, D. & Smith, G. D. Initial observation of grain boundary solute segregation in a zirconium alloy (ZIRLO) by three-dimensional atom probe. *Scripta Materialia* **61,** 411–414 (2009).
27. Lidiard, A. B. Atomic transport in solids: Models and their parameterization. *Solid State Ionics* **101-103,** 299–309 (1997).
28. Ramunni, V. P. Diffusion behavior in Nickel-Aluminum and Aluminum-Uranium diluted alloys. *Computational Materials Science* **93,** 112–124 (2014).
29. Mehrer, H. *Diffusion in Solids: Fundamentals, Methods, Materials, Diffusion-Controlled Processes* (Springer Berlin Heidelberg, 2007).
30. Messina, L., Nastar, M., Garnier, T., Domain, C. & Olsson, P. Exact ab initio transport coefficients in bcc Fe-X (X=Cr, Cu, Mn, Ni, P, Si) dilute alloys. *Physical Review B - Condensed Matter and Materials Physics* **90,** 1–15 (2014).
31. Trinkle, D. R. Diffusivity and derivatives for interstitial solutes: activation energy, volume, and elastodiffusion tensors. *Philosophical Magazine* **96,** 2714–2735 (2016).
32. Trinkle, D. R. Automatic numerical evaluation of vacancy-mediated transport for arbitrary crystals: Onsager coefficients in the dilute limit using a Green function approach. *Philosophical Magazine* **97,** 2514–2563 (2017).
33. Schuler, T., Messina, L. & Nastar, M. KineCluE: A kinetic cluster expansion code to compute transport coefficients beyond the dilute limit. *Computational Materials Science* **172,** 109191 (2020).
34. Bates, L. F. & Baqi, A. The magnetic properties of chromium. *Proceedings of the Physical Society* **48,** 781–794 (1936).
35. Steneteg, P., Alling, B. & Abrikosov, I. A. Equation of state of paramagnetic CrN from ab initio molecular dynamics. *Physical Review B - Condensed Matter and Materials Physics* **85,** 1–7 (2012).
36. Anisimov, V. I. & Lukoyanov, A. V. Investigation of real materials with strong electronic correlations by the LDA+DMFT method. *Acta Crystallographica Section C: Structural Chemistry* **70,** 137–159 (2014).
37. Kresse, G. & Furthmuller, J. Efficient iterative schemes for ab initio total-energy calculations using a plane-wave basis set. *Physical Review B - Condensed Matter and Materials Physics* **54,** 11169–11186 (1996).
38. Kresse, G. & Furthmuller, J. Efficiency of ab-initio total energy calculations for metals and semiconductors using a plane-wave basis set. *Computational Materials Science* **6,** 15–50 (1996).
39. Perdew, J. P., Burke, K. & Ernzerhof, M. Generalized gradient approximation made simple. *Physical Review Letters* **77,** 3865–3868 (1996).
40. Medvedeva, N. I., Gornostyrev, Y. N. & Freeman, A. J. Structural properties, electronic structure, Fermi surface, and mechanical behavior of bcc Cr-Re alloys. *Physical Review B - Condensed Matter and Materials Physics* **67,** 1–7 (2003).
41. Jiang, C., Wolverton, C., Sofo, J., Chen, L. Q. & Liu, Z. K. First-principles study of binary bcc alloys using special quasirandom structures. *Physical Review B - Condensed Matter and Materials Physics* **69,** 1–10 (2004).

42. Henkelman, G., Uberuaga, B. P. & Jónsson, H. Climbing image nudged elastic band method for finding saddle points and minimum energy paths. *Journal of Chemical Physics* **113,** 9901–9904 (2000).

43. Henkelman, G. & Jónsson, H. Improved tangent estimate in the nudged elastic band method for finding minimum energy paths and saddle points. *Journal of Chemical Physics* **113,** 9978–9985 (2000).

44. Vineyard, G. H. Frequency factors and isotope effects in solid state rate processes. *Journal of Physics and Chemistry of Solids* **3,** 121–127 (1957).

45. Burr, P. A. & Oliver, S. X. Formation and migration of point defects in tungsten carbide: Unveiling the sluggish bulk self-diffusivity of WC. *Journal of the European Ceramic Society* **39,** 165–172 (2019).

46. Nguyen-Manh, D., Dudarev, S. L. & Horsfield, A. P. Systematic group-specific trends for point defects in bcc transition metals: An ab initio study. *Journal of Nuclear Materials* **367-370 A,** 257–262 (2007).

47. Ma, P. W. & Dudarev, S. L. Effect of stress on vacancy formation and migration in body-centered-cubic metals. *Phys. Rev. Materials* **3,** 63601 (June 2019).

48. Schultz, H. *2.2.1 Special remarks: Datasheet from Landolt-Börnstein - Group III Condensed Matter · Volume 25: "Atomic Defects in Metals" in SpringerMaterials* (ed Ullmaier, H.) (Springer-Verlag Berlin Heidelberg).

49. Cerdeira, M. A., Palacios, S. L., González, C., Fernández-Pello, D. & Iglesias, R. Ab initio simulations of the structure, energetics and mobility of radiation-induced point defects in bcc Nb. *Journal of Nuclear Materials* **478,** 185–196 (2016).

50. Seletskaia, T., Osetsky, Y., Stoller, R. E. & Stocks, G. M. First-principles theory of the energetics of He defects in bcc transition metals. *Physical Review B - Condensed Matter and Materials Physics* **78,** 1–9 (2008).

51. Burton, J. J. Vacancy-Formation Entropy in Cubic Metals. *Phys. Rev. B* **5,** 2948–2957 (Apr. 1972).

52. Mundy, J. N., Hoff, H. A., Pelleg, J., Rothman, S. J., Nowicki, L. J. & Schmidt, F. A. Self-diffusion in chromium. *Physical Review B* **24,** 658–665 (1981).

53. Einziger, R. E., Mundy, J. N. & Hoff, H. A. Niobium self-diffusion. *Physical Review B* **17,** 440–448 (1978).

54. Park, M., Alexander, K. C. & Schuh, C. A. Diffusion of tungsten in chromium: Experiments and atomistic modeling. *Journal of Alloys and Compounds* **611,** 433–439 (2014).

55. Askill, J. & Tomlin, D. H. Self-diffusion in chromium. *Philosophical Magazine* **11,** 467–474 (1965).

56. Campbell, J. L. & Schulte, C. W. Positron trapping and self-diffusion activation energies in chromium. *Applied Physics* **19,** 149–152 (1979).

57. Peterson, N. L. Self-diffusion in pure metals. *Journal of Nuclear Materials* **69-70,** 3–37 (1978).

58. Lejaeghere, K., Van Speybroeck, V., Van Oost, G. & Cottenier, S. Error estimates for solid-state density-functional theory predictions: An overview by means of the ground-state elemental crystals. *Critical Reviews in Solid State and Materials Sciences* **39,** 1–24 (2014).

59. Moustafa, S. G., Schultz, A. J., Zurek, E. & Kofke, D. A. Accurate and precise ab initio anharmonic free-energy calculations for metallic crystals: Application to hcp Fe at high temperature and pressure. *Physical Review B* **96,** 1–13 (2017).

60. Einziger, R. E. & Mundy, J. N. Diffusion of zirconium in niobium: The influence of fast diffusing impurities on the self-diffusion isotope effect. *Phys. Rev. B* **17,** 449–454 (1978).

61. Xin, X. K., Lai, W. S. & Liu, B. X. Point defect properties in hcp and bcc Zr with trace solute Nb revealed by ab initio calculations. *Journal of Nuclear Materials* **393,** 197–202 (2009).

62. Kim, W. Y. & Takasugi, T. Laves phase fields in Cr-Zr-Nb and Cr-Zr-Hf alloy systems. *Scripta Materialia* **48,** 559–563 (2003).

63. Vainshtein, B. K., Fridkin, V. M. & Indenbom, V. L. in *Structure of Crystals* 330–399 (Springer Berlin Heidelberg, Berlin, Heidelberg, 1995).

64. Yip, S. *Handbook of Materials Modeling* (Springer Netherlands, 2007).

65. Derlet, P. M., Nguyen-Manh, D. & Dudarev, S. L. Multiscale modeling of crowdion and vacancy defects in body-centered-cubic transition metals. *Physical Review B - Condensed Matter and Materials Physics* **76,** 1–22 (2007).

66. Bocquet, J. L., Barouh, C. & Fu, C. C. Migration mechanism for oversized solutes in cubic lattices: The case of yttrium in iron. *Physical Review B* **95,** 1–11 (2017).

67. Lambert, D. S., Lennon, A. & Burr, P. A. Diffusion mechanisms of Mo contamination in Si. *Physical Review Materials* **4,** 1–12 (2020).

68. Pelleg, J. Diffusion of 51Cr into niobium single crystals. *Philosophical Magazine* **19,** 25–32 (1969).

69. Ablitzer, D. Diffusion of niobium, iron, cobalt, nickel and copper in niobium. *Philosophical Magazine* **35,** 1239–1256 (1977).

70. Soubeyroux, J. L., Bououdina, M., Fruchart, D. & Pontonnier, L. Phase stability and neutron diffraction studies of Laves phases Zr(Cr1-xMx)2 with M = Mn, Fe, Co, Ni, Cu and $0 < x < 0.2$ and their hydrides. *Journal of Alloys and Compounds* **219,** 48–54 (1995).

71. Sun, J. & Jiang, B. Ab initio calculation of the phase stability, mechanical properties and electronic structure of ZrCr2 Laves phase compounds. *Philosophical Magazine* **84,** 3133–3144 (2004).

72. Zhong, W., Mouche, P. A. & Heuser, B. J. Response of Cr and Cr-Al coatings on Zircaloy-2 to high temperature steam. *Journal of Nuclear Materials* **498,** 137–148 (2018).

73. Brachet, J. C., Rouesne, E., Ribis, J., Guilbert, T., Urvoy, S., Nony, G., Toffolon-Masclet, C., Le Saux, M., Chaabane, N., Palancher, H., David, A., Bischoff, J., Augereau, J. & Pouillier, E. High temperature steam oxidation of chromium-coated zirconium-based alloys: Kinetics and process. *Corrosion Science* **167,** 108537 (2020).